

Developing Single-Atomic Manganese Nanozymes for Synergistic Mild Photothermal/Multienzymatic Therapy

Cun-shuo Wang,¹ Hai-bin Xue,¹ Liang Zhuang,¹ Hai-peng Sun, Hua Zheng, Shuai Wang, Shan He,* and Xiao-bo Luo*



Cite This: *ACS Omega* 2023, 8, 49289–49301



Read Online

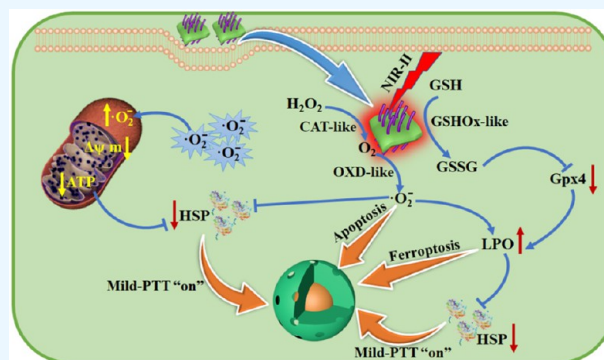
ACCESS |

Metrics & More

Article Recommendations

Supporting Information

ABSTRACT: Synergistic mild photothermal/nanozyme therapy with outstanding hyperthermia performance and excellent multienzyme properties is highly needed for osteosarcoma treatment. Herein, we have developed efficient single-atom nanozymes (SANs) consisting of Mn sites atomically dispersed on nitrogen-doped carbon nanosheets (denoted as Mn-SANs) for synergistic mild photothermal/multienzymatic therapy against osteosarcoma. Benefiting from their black N-doped carbon nanosheet matrices, Mn-SANs showed an excellent NIR-II-triggered photothermal effect. On the other hand, Mn-SANs with atomically dispersed Mn sites have outstanding multienzyme activities. Mn-SANs can catalyze endogenous H₂O₂ in osteosarcoma into O₂ by catalase (CAT)-like activity, which can effectively ease osteosarcoma hypoxia and trigger the oxidase (OXD)-like catalysis that converts O₂ to the cytotoxic superoxide anion radical ($\cdot\text{O}_2^-$). At the same time, Mn-SANs can also mimic glutathione oxidase (GSHOx) to effectively consume the antioxidant glutathione (GSH) in osteosarcoma and inhibit intracellular glutathione peroxidase 4 (GPX4) expression. Such intratumoral $\cdot\text{O}_2^-$ production, GSH depletion, and GPX4 inactivation mediated by Mn-SANs can create a large accumulation of lipid peroxides (LPO) and $\cdot\text{O}_2^-$, leading to oxidative stress and disrupting the redox homeostasis in osteosarcoma cells, which can ultimately induce osteosarcoma cell death. More importantly, heat shock proteins (HSPs) can be significantly destroyed via Mn-SAN-mediated plentiful LPO and $\cdot\text{O}_2^-$ generation, thus effectively impairing osteosarcoma cells resistant to mild photothermal therapy. Overall, through the cooperative effect of chemical processes (boosting $\cdot\text{O}_2^-$, consuming GSH, and enhancing LPO) and biological processes (inactivating GPX4 and hindering HSPs), collaborative mild photothermal/multienzymatic therapy mediated by Mn-SANs is a promising strategy for efficient osteosarcoma treatment.



1. INTRODUCTION

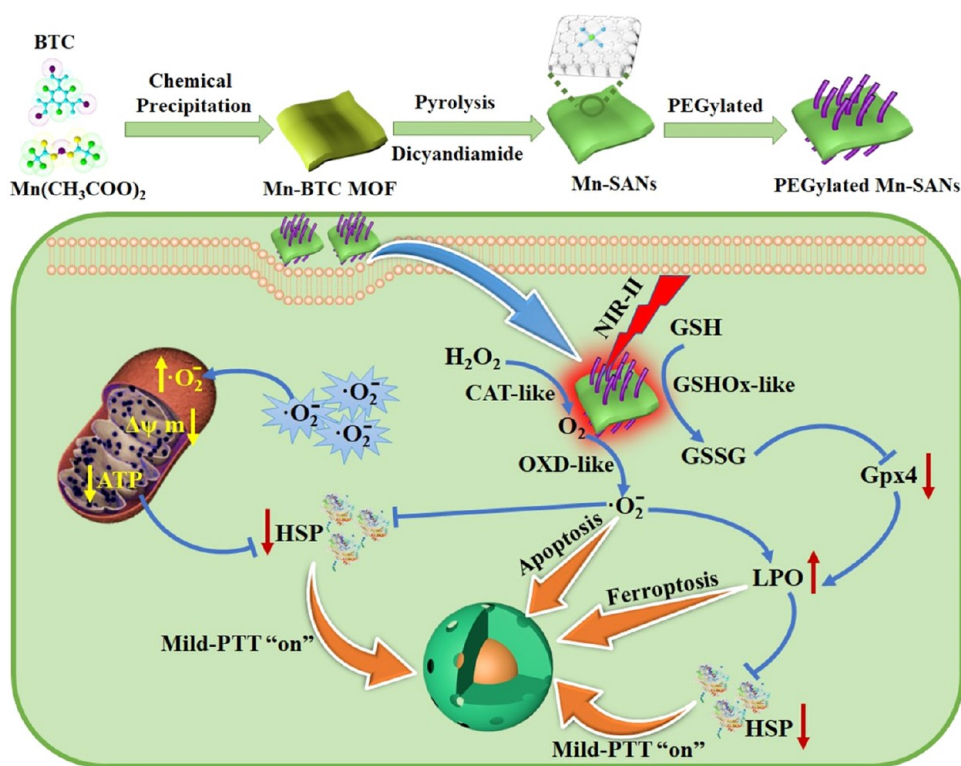
Osteosarcoma, as a type of tumor with high malignancy and easy recurrence and metastasis, greatly affects people's health and life, especially teenagers and young adults.^{1,2} With the progression of osteosarcoma, there may be very unsatisfactory prognosis, including pain, fractures, tumor recurrence, and metastasis.^{1–3} At present, the first choice for clinical treatment is wide-margin surgical resection of osteosarcoma.^{3,4} However, due to the complexity and high malignancy of osteosarcoma, the progression of osteosarcoma would be rapid, and limb-sparing surgery resection is not always applicable.^{1–4} Although chemotherapy against osteosarcoma has been developed, the poor responsiveness of tumor cells and the rapid emergence of drug resistance often impair the therapeutic effectiveness.^{1–4} Because of these clinical difficulties, osteosarcoma therapeutics with new mechanisms and highly efficient antitumor effects are highly desired. Photothermal therapy (PTT), which depends on photothermal nanoagents to generate cytotoxic heat for killing tumor cells with high specificity and efficiency under near-infrared (NIR) laser irradiation, is one of the most

effective therapeutic modalities for osteosarcoma treatment due to its minimal invasiveness, high tissue penetration, and prominent antitumor effects.^{1,5} Nevertheless, to realize entire tumor eradication, PTT needs to elevate the intratumoral temperature to above 50 °C.^{6–9} Such hyperthermia performance can not only induce tumor cell death but also cause an unavoidable damage to surrounding healthy tissues via the complexity in preventing heat diffusion.^{6–9} Besides, during PTT, inevitable adverse effects will be formed of inflammatory disease and systemic immune responses caused by the hyperthermia ablation.^{6–9} Compared with conventional PTT, the emerging mild PTT (lower than 45 °C) may successfully destroy primary osteosarcoma, while preventing thermal

Received: October 4, 2023
Revised: November 14, 2023
Accepted: November 28, 2023
Published: December 13, 2023



Scheme 1. Diagram of the Fabrication Process of the Mn-SANs and Their Mechanism for Synergistic Mild Photothermal/Multienzymatic Therapy



damage to normal tissues and alleviating unwanted inflammatory/immunosuppression.^{6,7} Nevertheless, the curative effects of mild PTT were severely impaired due to the upregulated expression of the heat shock proteins (HSPs), which would resist heat pressure and repair the thermally damaged tumor cells.^{10,11} In recent years, small-molecular HSP inhibitors, small-interfering RNA (siRNA), and nanosystems with photothermal agents binding HSP inhibitors or siRNA have been exploited to boost the curative effects of mild PTT.^{12–15} Nevertheless, they are usually not satisfying due to poor water solubility, high systemic toxicity, inferior stability, low loading efficiency, and especially asynchronous hysteretic therapeutic effects, thereby impeding the future clinic practice.^{7,16,17} Consequently, it is essential to develop a multifunctional nanomaterial as a therapeutic nanoagent that combines hyperthermia properties with HSP silencing to improve the therapeutic efficacy of mild PTT for osteosarcoma.

Recently, nanozymes with intrinsic enzyme-like characteristics have received growing attention in numerous disease treatments, including antitumor therapy, due to their low cost, easy storage, unique physicochemical properties, high penetrability, superior stability, and multifunctionalities.^{18–23} In particular, nanozyme-based therapy, in which nanozymes specifically in situ trigger enzymatic activity within the tumor microenvironment (TME) and catalyze oxidoreductase-mimic reactions to break relatively vulnerable homeostasis of tumors (especially redox homeostasis) for killing tumor cells, represents an emerging antitumor modality.^{21–25} Typically, transition metal-based nanozymes can effectively catalyze enzyme-like reactions (e.g., CAT-, OXD-, and POD-like reactions) with overexpressed H_2O_2 of the TME as the initial reactant to generate oxygen and cytotoxic reactive oxygen species (ROS, e.g., $\cdot\text{O}_2^-$ and $\cdot\text{OH}$).^{20–25} This can not only

alleviate hypoxia in the TME but also disrupt the redox homeostasis within the tumor and induce oxidative stress, ultimately causing severe oxidative damage to tumor cells.^{20,25–27} More importantly, abundant ROS production in the tumor subsequently leads to the enrichment of lipid peroxides (LPO), and the resulting ROS and LPO can crosslink primary amines of HSPs to damage their structure and efficacy, thereby inhibiting HSP expression and promoting mild PTT.^{6,28} Meanwhile, LPO accumulation can also induce ferroptosis for tumor cell killing.^{29,30} On the other side, nanozymes with glutathione oxidase (GSPOx)-like activity can catalyze the oxidation of glutathione (GSH, as the most important antioxidant) into glutathione disulfide (GSSG), thus reducing the GSH content in tumor cells and depressing the expression of glutathione peroxidase 4 (GPX4).^{6,29,30} Such depletion of GSH and inactivation of GPX4 can not only help destroy the intracellular redox balance but also facilitate the accumulation of LPO and ROS in the tumor, further cleaving HSPs and improving mild PTT as well as boosting ferroptosis.^{6,29,30} Notably, mild heating can also enhance oxidoreductase-like activities and accelerate intratumoral homeostasis disruption.^{1,6,7,31} Therefore, building a synergistic mild photothermal/nanozyme therapy is a promising strategy to enhance mild PTT performance and achieve synergistic antiosteosarcoma efficacy. Nevertheless, because only a small segment of active-site atoms exposed to the surface can devote to the enzyme-like catalysis, nanozymes face the severe challenge of catalytic activity, which extremely influences the therapeutic efficacy of nanozymes. Meanwhile, how to rationally scheme efficient nanozymes with multienzyme properties and NIR light response simultaneously to achieve synergistic enhanced mild photothermal/nanozyme therapy is another challenge.

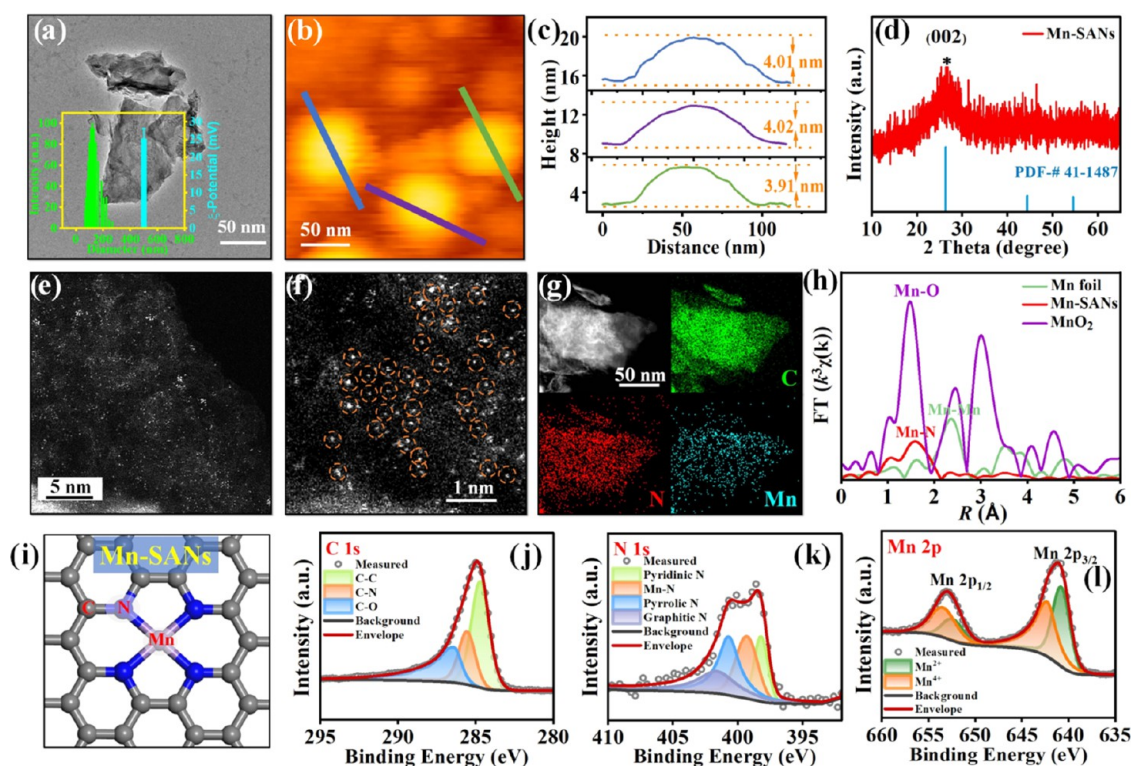


Figure 1. (a) TEM image of the Mn-SAN sample. (b) AFM image and (c) corresponding height profile of Mn-SANs. (d) XRD pattern of Mn-SANs. (e, f) AC-HAADF-STEM images of Mn-SANs (orange dashed circle-marked Mn single atoms in Mn-SANs). (g) EDX elemental mapping of Mn-SANs. (h) FT of the k^3 -weighted EXAFS spectra at the Mn K-edge of Mn-SANs. The FT was not corrected for the phase shift. (i) Schematic illustration of the coordination structure for Mn-SANs. Deconvoluted C 1s XPS spectra (j) and N 1s XPS spectra (k) for Mn-SANs. (l) Mn 2p XPS spectra for Mn-SANs.

Single-atom nanozymes (SANs) are very promising antitumor nanoagents owing to their adjustable electronic and geometric structures, maximum atomic utilization efficiency, atomically dispersed active sites, and outstanding catalytic activities.^{6,26–28,31} Specifically, the SANs consist of nitrogen-doped carbon matrices with anchored single metal atoms and exert multiple functionalities, including superior NIR light absorption, promotion of osteoinduction by nitrogen-doped carbon matrices, and exertion of multienzyme activities.^{32–34} However, most of the previously reported nitrogen-doped carbon matrices for holding single-atom sites present three-dimensional bulk structures, rendering a large amount of active sites buried inside and restricting mass transfer during the catalytic reaction.³⁵ Forming 2D nitrogen-doped carbon matrices is an attractive strategy that can fully expose the active sites and accelerate mass transfer during the reaction process.³⁶ Meanwhile, the 2D structure might permit nitrogen-doped carbon matrices to serve as laser-cavity mirrors, which would improve the NIR light absorption and photothermal conversion efficiency.³⁷ Herein, we developed multifunctional SANs consisting of Mn single-atom sites anchored on 2D nitrogenated carbon nanosheets (denoted as Mn-SANs) for synergistic mild photothermal/multienzymatic therapy against osteosarcoma (Scheme 1). The resulting Mn-SANs showed a remarkable photothermal effect in the near-infrared II (NIR-II, 1000–1400 nm) region and had excellent synergistic multienzyme properties. On the one hand, owing to their black N-doped carbon nanosheet matrices, Mn-SANs possessed strong optical absorption and exhibited excellent NIR-II-triggered photothermal performance. Moreover, by adjusting laser power density, Mn-SANs can give a relatively

safe mild treatment temperature. On the other hand, Mn-SANs can catalyze endogenous H_2O_2 in osteosarcoma into O_2 by CAT-like activity, excellently easing osteosarcoma low oxygen conditions and activating the OXD-like catalysis that converted O_2 to cytotoxic $\cdot\text{O}_2^-$. At the same time, Mn-SANs can also mimic GSHOx to effectively consume the antioxidant GSH in the TME and inhibit intracellular GPX4 expression. Such intratumoral $\cdot\text{O}_2^-$ production, GSH depletion, and GPX4 inactivation mediated by Mn-SANs can create a large accumulation of LPO and $\cdot\text{O}_2^-$, leading to oxidative stress and disrupting the redox homeostasis in tumor cells, which ultimately induced tumor cell death. More importantly, HSPs can be significantly destroyed through Mn-SAN-mediated plentiful LPO and ROS generation, thus effectively impairing tumor cells resistant to mild PTT. Additionally, the photothermal effect triggered by Mn-SANs can further enhance multienzyme synergistic catalysis to heighten $\cdot\text{O}_2^-$ production, GSH depletion, and LPO accumulation. Finally, through a two-pronged strategy of chemical trails (boosting $\cdot\text{O}_2^-$, exhausting GSH, and promoting LPO) and biological processes (inactivating GPX4 and hindering HSPs), a synergistic mild photothermal/multienzymatic therapy mediated by Mn-SANs exhibited a significantly enhanced antiosteosarcoma efficacy.

2. RESULTS AND DISCUSSION

The preparation process, using the pyrolysis strategy of the metal–organic framework (MOF) precursor, for Mn-SANs with N-doped carbon nanosheet morphology is shown in Scheme 1. As shown in the transmission electron microscopy

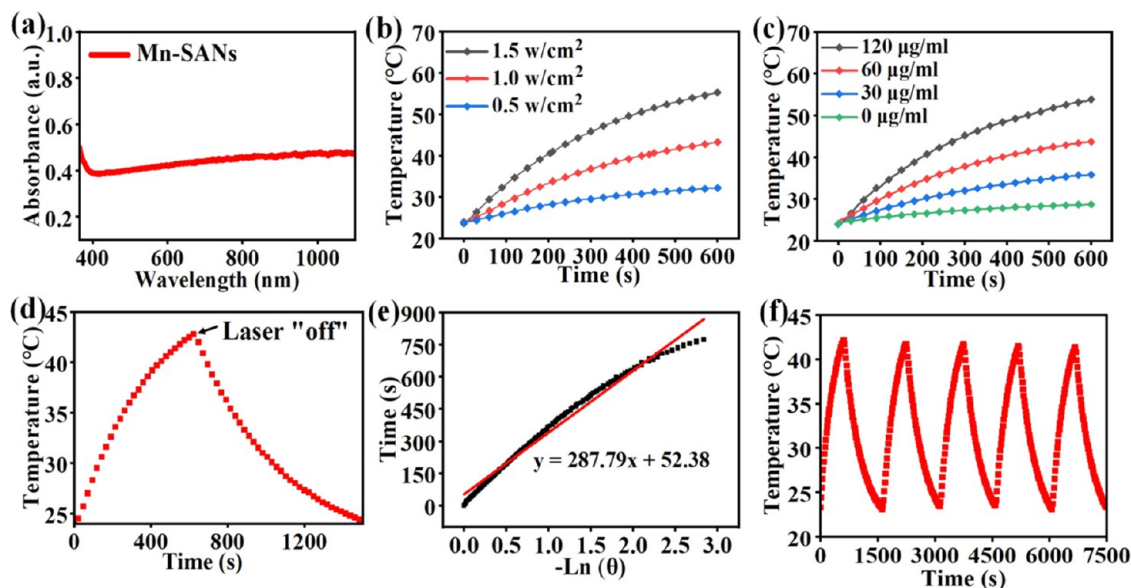


Figure 2. (a) UV–vis–NIR absorption spectrum of Mn-SANs. (b) Temperature elevation curve of Mn-SANs ($60 \mu\text{g mL}^{-1}$) (variation power density of the NIR-II laser). (c) Temperature elevation curve of Mn-SANs with different concentrations under 1.0 W cm^{-2} of the NIR-II laser. (d) Heating and cooling curve of Mn-SANs under 1064 nm laser irradiation. (e) Cooling time versus $-\ln \theta$ fitted by a linear equation. (f) Thermal stability of Mn-SANs.

(TEM) image, Mn-SANs presented a typical nanosheet morphology (Figure 1a). Moreover, the average size of Mn-SANs was $\sim 122 \text{ nm}$, as revealed by dynamic light scattering (DLS) (Figure S1). Meanwhile, the thickness of Mn-SANs was detected to be $\sim 4.0 \text{ nm}$ via atomic force microscopy (AFM), further identifying their nanosheet structure for Mn-SANs (Figure 1b,c). Such a 2D nanosheet structure was advantageous for the adequate exposure of Mn active centers and promoted mass transfer through catalyst layers, thereby enhancing catalytic activity and improving reaction kinetic features.³⁶ Moreover, the X-ray diffraction (XRD) pattern revealed that Mn-SANs presented two diffraction peaks that can be attributed to the (002) and (101) planes of graphite-like carbon at 26.3 and 42.9° (PDF 41-1487), respectively, while no peaks from metal or metallic oxide nanoparticles can be detected (Figure 1d). This indicated the nonappearance of Mn-based nanoelectrons in Mn-SANs, which was in accordance with the TEM observations. Atomically dispersed Mn sites in Mn-SANs were further confirmed by careful aberration-corrected high-angle annular dark-field scanning transmission electron microscopy (AC-HAADF-STEM) analyses. As presented in Figure 1e, the numerous bright spots were homogeneously dispersed on the N-doped carbon nanosheets, indicating the uniform dispersion of metal single atoms. The enlarged AC-HAADF-STEM image further confirmed that Mn single atoms (emphasized by orange loops) existed in Mn-SANs (Figure 1f). Correspondingly, it was found that C, N, and Mn atoms were homogeneously dispersed in Mn-SANs, as revealed by energy dispersive X-ray spectroscopy (EDX) elemental mapping analyses (Figure 1g). Additionally, the weight loadings of Mn in the Mn-SANs were $\sim 4.21\%$, as revealed by inductively coupled plasma atomic emission spectroscopy (ICP-AES).

Next, the extended X-ray absorption fine structure (EXAFS) was performed to investigate the fine structure of Mn-SANs. The Fourier transform (FT) of the EXAFS spectra at the Mn K-edge for Mn-SANs exhibited a prominent peak around ~ 1.6

\AA (Figure 1h), belonging to Mn–N scattering paths (Figure 1i). Notably, compared to Mn foil, no measurable first Mn–Mn shell peak at $\sim 2.3 \text{ \AA}$ was observed in Mn-SANs, suggesting that atomically dispersed Mn sites were anchored on the N-doped carbon nanosheets. Furthermore, the electronic structure of the Mn-SANs was investigated using high-resolution X-ray photoelectron spectroscopy (XPS). The deconvoluted C 1s peak attributed to the C–N bonding was observed at 285.5 eV , suggesting the existence of N-doped carbon species in Mn-SANs (Figure 1j).³⁸ Meanwhile, the N 1s XPS of Mn-SANs can be deconvoluted into four peaks, which were assigned to graphitic N, pyrrolic N, Mn–N, and pyridinic N (Figure 1k).³⁹ These results suggested that the Mn atoms in Mn-SANs are basically coordinated with the N sites of the nitrogenated carbon nanosheets. Moreover, the Mn $2p_{3/2}$ spectrum displayed the presence of Mn^{2+} (640.9 eV) and Mn^{4+} (642.3 eV) species in Mn-SANs (Figure 1l).⁴⁰ Therefore, a combination study including XRD, AC-HAADF-STEM, EXAFS, and XPS confirmed the successful fabrication of Mn single atoms on the N-doped carbon nanosheets.

2.1. Synergistic Photothermal Performance and Multienzyme-Mimicking Properties. Mild-temperature photothermal therapy, which depended on the photothermal conversion agent to produce cytotoxic heat ($<45^\circ \text{C}$) under near-infrared (NIR) laser irradiation, was a promising noninvasive and stimuli-responsive therapeutic modality for destroying tumor cells and preventing normal tissue from destruction by excessive temperature.^{6,7} Meanwhile, NIR-II light-triggered photothermal therapy (NIR-II region: $1000\text{--}1700 \text{ nm}$) can achieve an outstanding therapeutic effect for deep tumor treatment, owing to the stronger tissue penetration and lower scattering of NIR-II light.^{41,42} Here, the UV–vis–NIR absorption spectrum of Mn-SANs (Figure 2a) displayed a flat and stretchable absorption band in the NIR region ($>780 \text{ nm}$), suggesting their significant NIR-II light absorption. Encouraged by this, 1064 nm was utilized as a light source to explore the NIR-II light-triggered photothermal perform-

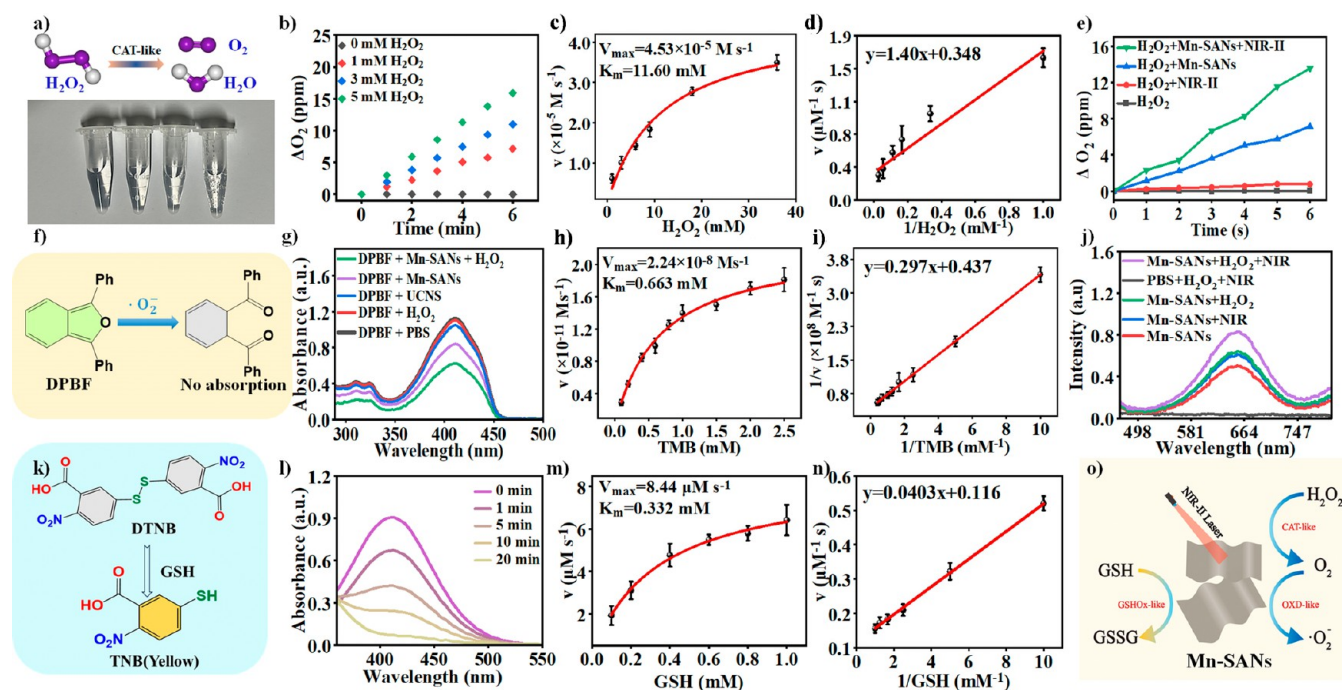


Figure 3. (a) Reaction scheme for H_2O_2 decomposition and photos displaying O_2 production under different treatments at pH 6.0: PBS, H_2O_2 , $\text{H}_2\text{O}_2 + \text{UCNs}$, and $\text{H}_2\text{O}_2 + \text{Mn-SANs}$. (b) O_2 production from H_2O_2 decomposition by Mn-SAN-mediated catalysis under different H_2O_2 concentrations. (c) Michaelis–Menten kinetic analysis and (d) Lineweaver–Burk plot for CAT-like action of Mn-SANs with H_2O_2 as the substrate. (e) NIR-II laser-enhanced CAT-like catalysis and corresponding O_2 generation by Mn-SANs. (f) Reaction scheme for $\cdot\text{O}_2^-$ -induced DPBF oxidation through OXD-like catalysis. (g) UV–vis spectrum of different treatments for DPBF oxidation at pH 6.0: DPBF + PBS, DPBF + H_2O_2 , DPBF + UCNS, DPBF + Mn-SANs, and DPBF + Mn-SANs + H_2O_2 . (h) Michaelis–Menten kinetic analysis and (i) Lineweaver–Burk plot for the OXD-like action of Mn-SANs with TMB as the substrate. (j) NIR-II laser-enhanced OXD-like catalytic activity and corresponding $\cdot\text{O}_2^-$ generation by Mn-SANs. (k) Schematic diagram of the reaction mechanism of GSH and DTNB. (l) GSH consumption after treatment with Mn-SANs. (m) Michaelis–Menten kinetic analysis and (n) Lineweaver–Burk plot for GSHOx-like action of Mn-SANs with GSH as a substrate. (o) Schematic illustration of Mn-SANs for the photothermal-synergistic multienzyme-mimicking reaction.

ance of Mn-SANs. Initially, photothermal performance was examined by detecting the temperature elevation of Mn-SANs under 1064 nm (varying power intensity) (Figure 2b). Mn-SANs exhibited a power density-dependent heating behavior. Moreover, the Mn-SANs displayed raised temperature with increasing concentration, and the temperature can reach 53.8 °C after irradiation with a 1064 nm laser for 10 min (Figure 2c). By contrast, the temperature of pure water only elevated to 28.7 °C under the same conditions. Notably, the photothermal conversion efficiency (η) of Mn-SANs was determined to be 40.3% (Figure 2d,e). In addition, after five consecutive heating/cooling cycles, there was no significant change in the photothermal performance of Mn-SANs, confirming their stable photothermal properties (Figure 2f). Besides, UCNS exhibited photothermal behavior like that of Mn-SANs (Figure S2). Therefore, the Mn-SANs can act as an ideal photothermal agent for NIR-II light-triggered mild photothermal therapy and cause local heat to improve their synergistic multienzyme-mimicking catalysis.

Next, the catalase (CAT)-, oxidase (OXD)-, and glutathione oxidase (GSHOx)-like properties of Mn-SANs were investigated in the mimic mildly acidic TME (pH 6.0). Mn-SANs can efficiently catalyze the conversion of H_2O_2 to O_2 , as revealed by generating gas bubbles in solution when Mn-SANs and H_2O_2 were present (Figure 3a). Meanwhile, with the increase of H_2O_2 concentration, Mn-SANs exhibited enhanced ability to decompose H_2O_2 into O_2 , identifying the outstanding CAT-like activity of Mn-SANs (Figure 3b). On the contrary, the UCNS under the same conditions failed to induce an

obvious generation of gas bubbles and showed negligible CAT-like activity; thus, Mn was indispensable for the catalysis. Moreover, based on the Michaelis–Menten equation, the Michaelis–Menten constant (K_m) and maximum reaction velocity (V_{\max}) during the CAT-like catalysis of Mn-SANs were calculated as 11.60 mM and $4.53 \times 10^{-5} \text{ M s}^{-1}$, respectively (Figure 3c). Furthermore, the CAT-like action of Mn-SANs was also fitted using the Lineweaver–Burk model (Figure 3d). In addition, the ability of Mn-SANs to decompose H_2O_2 into O_2 can be enhanced obviously under NIR-II irradiation, attributing to that their photothermal effect-induced temperature elevation boosted CAT-like catalysis (Figure 3e).^{25,43–47} Thus, Mn-SANs can efficaciously ease tumor hypoxia and create the prerequisite for triggering an OXD-like activity and generating cytotoxic $\cdot\text{O}_2^-$.

Oxidase, as one of the oxidative metalloenzymes, catalyzed the oxidation of substrate O_2 as an electron acceptor to cytotoxic $\cdot\text{O}_2^-$.²⁰ Furthermore, the possible $\cdot\text{O}_2^-$ generated by the OXD-like catalysis of Mn-SANs was measured using 1,3-diphenylisobenzofuran (DPBF) as the probe, as the absorbance of DPBF at 410 nm can be bleached by $\cdot\text{O}_2^-$ (Figure 3f). As shown in Figure 3g, the H_2O_2 or UCNS were found to have a very weak influence on DPBF oxidative bleaching. By contrast, significant DPBF oxidative bleaching was observed in the presence of Mn-SANs, and addition of H_2O_2 can further boost the oxidative bleaching of DPBF by Mn-SANs. Thus, $\cdot\text{O}_2^-$ was effectively produced through the OXD-like catalysis of Mn-SANs; it also confirmed O_2 generation through CAT-like catalysis of Mn-SANs, which

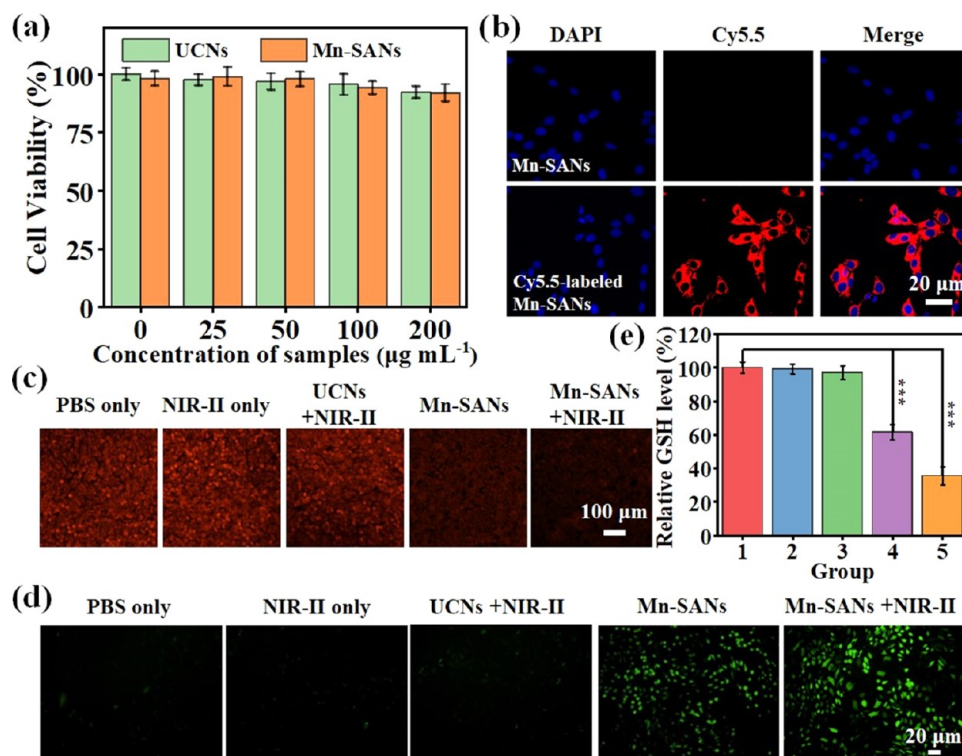


Figure 4. (a) Survival of L929 cells after the incubation with Mn-SANs and UCNs at various concentrations (ranging from 0, 25, 50, 100 $\mu\text{g mL}^{-1}$ to 200 $\mu\text{g mL}^{-1}$). (b) CLSM images for cellular uptake of Mn-SANs without any label (as control) in Saos-2 cells and Cy5.5-labeled Mn-SANs in Saos-2 cells. (c) O_2 release inside the cells detected by RDPP probe. (d) Intracellular $\cdot\text{O}_2^-$ detections of Saos-2 cells using DCFH-DA as the probe. (e) Intracellular GSH detections of Saos-2 cells with various groups: (1) PBS only, (2) NIR-II only, (3) UCNs + NIR-II, (4) Mn-SANs, and (5) Mn-SANs + NIR-II groups. ($n = 3$, mean \pm SD; $***p < 0.001$, $**p < 0.01$, and $*p < 0.05$).

can enhance subsequent OXD-like catalysis. The kinetic K_m and V_{\max} parameters were 0.66 mM and $2.24 \times 10^{-8} \text{ M s}^{-1}$ for OXD-like activity of Mn-SANs with 3,3',5,5'-tetramethylbenzidine (TMB) as a substrate, respectively (Figure 3h). Moreover, the OXD-like action of Mn-SANs was also fitted using the Lineweaver–Burk model (Figure 3i). Additionally, under 1064 nm laser irradiation, Mn-SANs can obviously promote the catalytic oxidation of TMB to the oxidized-TMB (blue product), as revealed by the significant enhancement in the absorbance at 652 nm (Figure 3j). This was attributed to that the photothermal effect-induced temperature elevation enhanced OXD-like catalysis of Mn-SANs, promoting $\cdot\text{O}_2^-$ generation.^{25,43–47} The generation of $\cdot\text{O}_2^-$ can further be boosted by 1064 nm laser plus H_2O_2 , suggesting that the photothermal effect of Mn-SANs enhanced multienzyme-mimicking synergistic catalysis. Since the TME was typically hypoxic while containing overexpressed H_2O_2 , a successive cascade reaction can proceed by multienzyme-like catalysis of Mn-SANs: Mn-SANs can decompose H_2O_2 into O_2 , followed by altering O_2 to $\cdot\text{O}_2^-$. Therefore, the $\cdot\text{O}_2^-$ produced by such cascade catalysis, by means of intratumoral excess H_2O_2 as the initial reactant, can induce oxidative stress and disorder the redox homeostasis, causing tumor cell death.

Notably, the overproduced glutathione (GSH) in tumor cells can extremely neutralize the generated ROS, thus greatly impairing oxidative damage to tumor cells.^{6,29} Moreover, glutathione peroxidase 4 (GPX4) could be inactivated by the depletion of GSH, causing the accumulation of lethal LPO triggered by ROS and thus inducing tumor cell death.^{6,29} Therefore, we investigated whether the Mn-SANs can mimic GSHOx to consume GSH. After the addition of Mn-SANs into

the GSH solution, the remnant GSH was detected by the probe 5,5'-dithiobis-2-nitrobenzoic acid (DTNB), which can react with GSH to generate TNB with a characteristic absorption peak at 412 nm (Figure 3k). It was observed that the absorbance at 412 nm decreases significantly with time, suggesting the oxidative consumption of GSH by GSHOx-mimicking activity of Mn-SANs (Figure 3l). Moreover, the Mn-SANs exhibited Michaelis–Menten kinetics during GSHOx-like action, and the kinetic K_m and V_{\max} parameters were calculated as 0.33 mM and $8.44 \times 10^{-6} \text{ M s}^{-1}$, respectively (Figure 3m). In addition, the GSHOx-like action of Mn-SANs was also fitted using the Lineweaver–Burk model (Figure 3n). Altogether, Mn-SANs can act as mild hyperthermia-reinforced multienzyme-mimic single-atom nanozymes to effectively alleviate tumor hypoxia and cause intracellular $\cdot\text{O}_2^-$ augmentation and oxidative damage to tumor cells (Figure 3o). Meanwhile, such intracellular $\cdot\text{O}_2^-$ augmentation can also severely destroy heat shock proteins (HSPs) that impede mild photothermal therapy.

2.2. In Vitro Synergistic Antiosteosarcoma Effect. To ensure the Mn-SANs with better biocompatibility and biosafety, mPEG-COOH was employed to modify the surface of Mn-SANs, ultimately obtaining PEGylated Mn-SANs. The successful surface modification of mPEG-COOH was confirmed through a change in the negative ζ -potential value (Figure S3). The resulting PEGylated Mn-SANs were well-dispersed in different physiological conditions: no obvious aggregation was found after PEGylated Mn-SANs were aged after 10 days, and the average size of PEGylated Mn-SANs also had no obvious change (Figure S4). Moreover, no Mn leach was detected in mildly acidic physiological medium (Figure

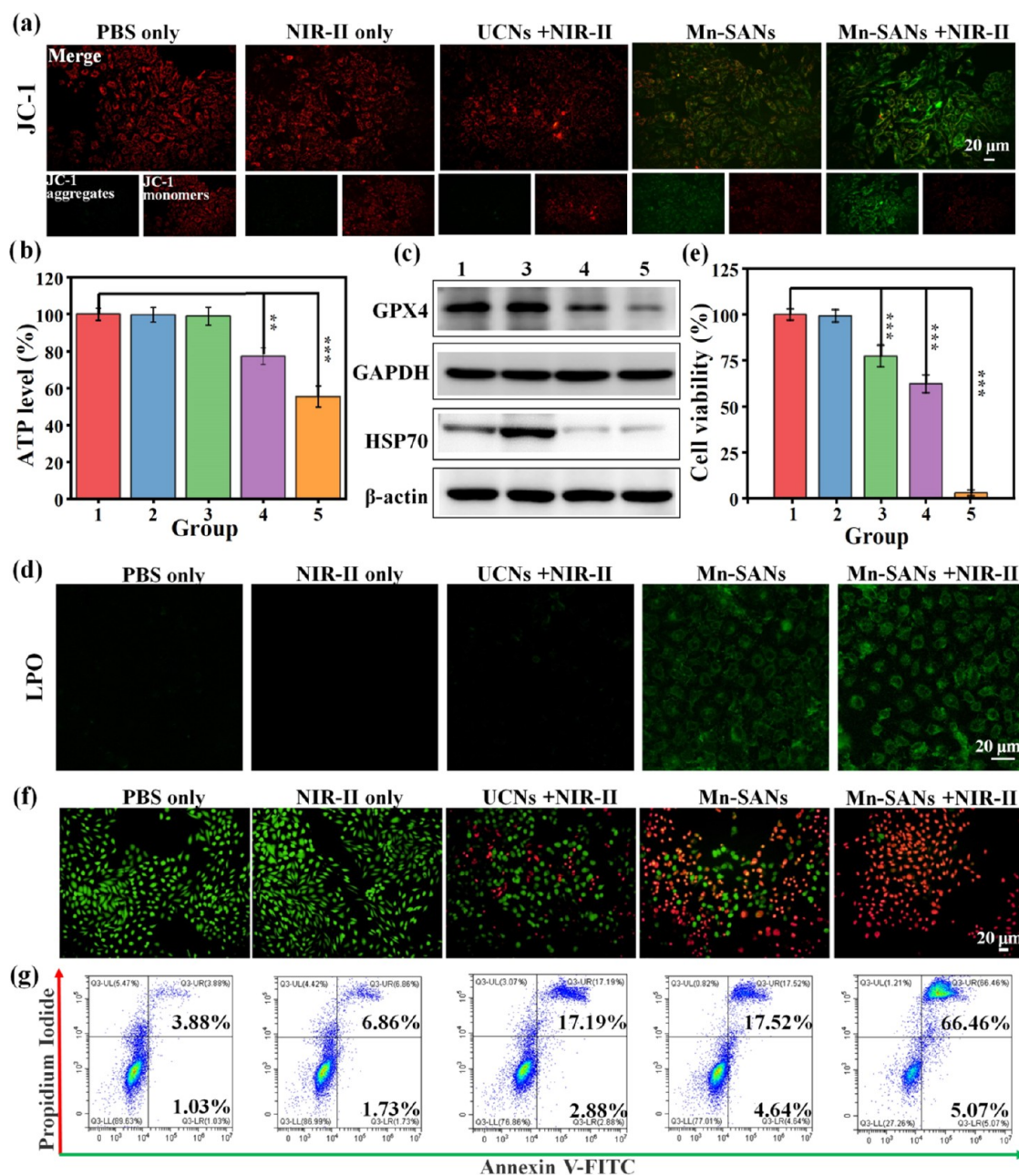


Figure 5. (a) Mitochondrial membrane potential of Saos-2 cells after staining by the JC-1 probe. (b) ATP level in Saos-2 cells with various treatments. (c) Western blots of GPX4 and HSP70 after various treatments. (d) Intracellular LPO detection using Liperfluor as a probe. (e) Cytotoxicity assessment on Saos-2 cells with different treatments. (f) Fluorescence imaging of calcein-AM/PI-stained Saos-2 cells after various treatments. (g) Flow cytometry results of Saos-2 cell apoptosis after various treatments. Groups: (1) PBS-only, (2) NIR-II-only, (3) UCNs + NIR-II, (4) Mn-SANs, and (5) Mn-SANs + NIR-II groups. ($n = 3$, mean \pm SD; *** $p < 0.001$, ** $p < 0.01$, and * $p < 0.05$).

SS). Besides, no significant differences were found between PEGylated Mn-SANs and Mn-SANs in terms of photothermal performance and multienzyme activities (Figure S6). These results indicated that PEGylated Mn-SANs possessed good stability under mildly acidic physiological conditions and maintained excellent photothermal/multienzymatic performance, thus enabling the application of biological experiments. To make it straightforward, the PEGylated Mn-SANs were referred to simply as Mn-SANs in the following text. Next, to reveal the cytocompatibility of Mn-SANs and UCNs, cell counting kit-8 (CCK-8) assay of fibroblast L929 cells was performed. As presented in Figure 4a, no evident toxicity of Mn-SANs and UCNs can be observed even at high

concentrations of $200 \mu\text{g mL}^{-1}$, suggesting their good biocompatibility. Endocytosis of Mn-SANs in osteosarcoma cells (Saos-2 cell line) was considered via confocal laser scanning microscopy (CLSM). After 4 h of incubation with Cy5.5-labeled Mn-SANs, Saos-2 cells displayed a red signal, while the nucleus showed blue intensity, suggesting that Cy5.5-labeled Mn-SANs were successfully ingested into Saos-2 cells and mainly accumulated in the cytoplasm (Figure 4b).

Encouraged by these superior photothermal performance and multienzyme properties of Mn-SANs, a synergistic mild photothermal and nanozyme therapeutic effect at the cellular level was studied in mimicking the tumor physiologic conditions (typically, $\text{pH} = 6.0$ and $100 \mu\text{M H}_2\text{O}_2$). The

Saos-2 cells were then treated with PBS-only, NIR-II-only, UCNs + NIR-II, Mn-SANs, and Mn-SANs + NIR-II groups. Initially, after different treatments of Saos-2 cells, intracellular O_2 levels were evaluated using the red fluorescent probe $[Ru(dpp)_3]Cl_2$ (RDPP). Compared with PBS-only, NIR-II-only, or UCNs + NIR-II groups, an obvious increase in intracellular O_2 levels was found in Saos-2 cells treated with Mn-SANs, confirmed by a noteworthy diminishment in intracellular red fluorescence of the RDPP probe (Figure 4c). This suggested that the Mn-SANs maintained the effective CAT-like activity in the Saos-2 cells. Notably, such an O_2 generation for Mn-SANs can be further heightened by NIR-II laser irradiation, attributed to the enhancement of CAT-like catalysis by their own photothermal effect. Such CAT-like activity of Mn-SANs, thus, can provide a prerequisite for effectively triggering OXD-like activity and generating cytotoxic $\bullet O_2^-$ in the hypoxic while H_2O_2 -rich TME. Then, the green fluorescent probe 2, 7-dichlorofluorescein diacetate (DCFH-DA) was used to detect intracellular $\bullet O_2^-$ generation. As presented in Figure 4d, evident DCFH-DA green fluorescence can be viewed in Saos-2 cells after treatment with Mn-SANs, suggesting that Mn-SANs can produce $\bullet O_2^-$ in cells through OXD-like catalysis, while intracellular $\bullet O_2^-$ generation was negligible in the PBS-only, NIR-II-only, or UCNs + NIR-II treatment group. Moreover, intracellular $\bullet O_2^-$ generation properties of Mn-SANs can be further enhanced after 1064 nm NIR-II laser irradiation due to their own photothermal effect. Meantime, it can be found that the Mn-SANs + NIR-II treatment group (Figure 4e) showed more pronounced consumption of intracellular GSH compared with the Mn-SAN group. This indicated that the photothermal effect can also heighten the GSHOx-like activity of Mn-SANs. Therefore, synergistic multienzyme-mimicking catalysis of Mn-SANs enhanced by a photothermal effect can break intracellular redox homeostasis and trigger the irreversible oxidative damage of $\bullet O_2^-$ to intracellular biomolecules (including proteins, nucleic acids, and lipids), ultimately inducing cell death.

The increased cellular ROS level can typically destroy the mitochondrial membrane and induce mitochondrial dysfunction, thereby causing a significant decrease in adenosine triphosphate (ATP) production and severe cell damage.^{25,31,48,49} We investigated Mn-SAN-mediated mitochondrial dysfunction using a 5',5',6,6'-tetrachloro-1,1',3,3'-tetraethyl-imidacarbocyanine iodide (JC-1) probe to indicate the loss of mitochondrial membrane potential (MMP) (Figure 5a). Compared to the PBS-only, NIR-II-only, or UCNs + NIR-II group, the increased disruption of the mitochondrial membrane was found in Saos-2 cells after treating with Mn-SANs, which decreased the red fluorescence and led to obvious green fluorescence. This was because the mitochondria were adversely affected by $\bullet O_2^-$ generation and GSH depletion mediated by the OXD- and GSHOx-like catalysis of Mn-SANs. Furthermore, the combination of NIR-II laser irradiation nearly depleted the red fluorescence and showed strong green fluorescence, suggesting the severe damage of the mitochondrial respiratory chain and mitochondrial membrane. Subsequently, it was also observed that the intracellular ATP production in the Mn-SANs + NIR-II-treated group was obviously inhibited compared with the cells in the other groups, due to the serious mitochondrial dysfunction of Saos-2 cells, originating from the synergies of the photothermal effect and multienzyme catalysis (Figure 5b). Accordingly, Mn-SANs

had the ability to disrupt the mitochondrial function and ATP synthesis, eventually leading to cell death.

The elevated intracellular ROS level can also cause serious oxidation of the cellular lipid by adding oxygen at the unsaturated bonds of fatty acid existing in the cellular lipid, thus inducing significant lipid peroxides (LPO) and cumulative ferroptosis.^{6,29,30} However, intracellular GSH and glutathione peroxidase 4 (GPX4) can reduce LPO accumulation and suppress ferroptosis in tumor cells.^{6,29,30} It was well known that the depletion of GSH can inhibit the expression of GPX4.^{6,29,30} Inspired by Mn-SAN-mediated effective GSH depletion (as shown in Figure 4e), we measured the expression of GPX4 in Saos-2 cells after different treatments. From western blot analysis, it was observed that the treatment of the Mn-SAN group can obviously inhibit the GPX4 level in Saos-2 cells compared to PBS only or the UCNs + NIR-II group, due to the oxidative consumption of GSH by GSHOx-mimicking activity of Mn-SANs (Figure 5c). Moreover, the Mn-SANs + NIR-II treatment group can further downregulate the GPX4 expression to a very low level, implying that photothermal effect-enhanced GSHOx-like catalysis can profoundly deplete GSH and effectively inactivating GPX4. Subsequently, it can be found that Mn-SANs irradiated by the NIR-II laser exhibited a significant accumulation of intracellular LPO, confirmed by strong green fluorescence of Liperfluo as an LPO probe (Figure 5d). Thus, these results demonstrated that the synergies of the photothermal effect and multienzyme catalysis mediated by Mn-SANs (enhancing ROS, depleting GSH, and inactivating GPX4) led to a plentiful accumulation of LPO in Saos-2 cells, triggering the ferroptosis process.

Notably, ROS generation and the collection of LPO can provide a strong method for slicing HSPs.^{6,28} The production of plentiful ROS can crosslink primary amines of HSPs to damage their structure and efficacy, while LPO can react with HSPs to form lethal crosslinks.^{6,28} Moreover, HSPs were ATP-dependent activated, and reducing ATP production can suppress the synthesis of HSPs and impair the HSP expression.^{28,49} It is worth noting that the downregulation of the HSP expression can sensitize tumor cells to mild photothermal therapy, considerably developing the healing efficiency.^{28,49} Thus, the inhibitory effect of Mn-SAN-mediated multienzyme catalysis on HSP expression was evaluated by western blotting assay to scrutinize the level of HSP70 in Saos-2 cells. It was found that the HSP70 content in Saos-2 cells treated with the UCNs + NIR-II group was notably superior than that of the PBS-only group, owing to that the generated mild photothermal effect activated upregulation of HSP expression (Figure 5c). For the Saos-2 cells treated with the Mn-SAN group, the HSP70 was obviously downregulated, representing that Mn-SAN-mediated ROS generation, LPO accumulation, and ATP decline inhibited HSPs. Positively, the HSP70 expression was still at a low level after the Mn-SANs were exposed to NIR-II irradiation, which made it tremendously possible for Mn-SAN-mediated multienzyme catalysis to boost mild PTT. Therefore, the above-mentioned results clearly indicated that the synergetic effect of ROS generation, LPO accumulation, and ATP decline mediated by the multienzyme catalysis of Mn-SANs can restrain HSP expression, which offered a potential strategy for improving mild PTT. Next, the therapeutic effect of synergistic mild photothermal/multienzymatic therapy was evaluated by CCK-8 assay (Figure 5e). Compared with the PBS-only group and NIR-II group, the UCNs + NIR-II group led to some lethality

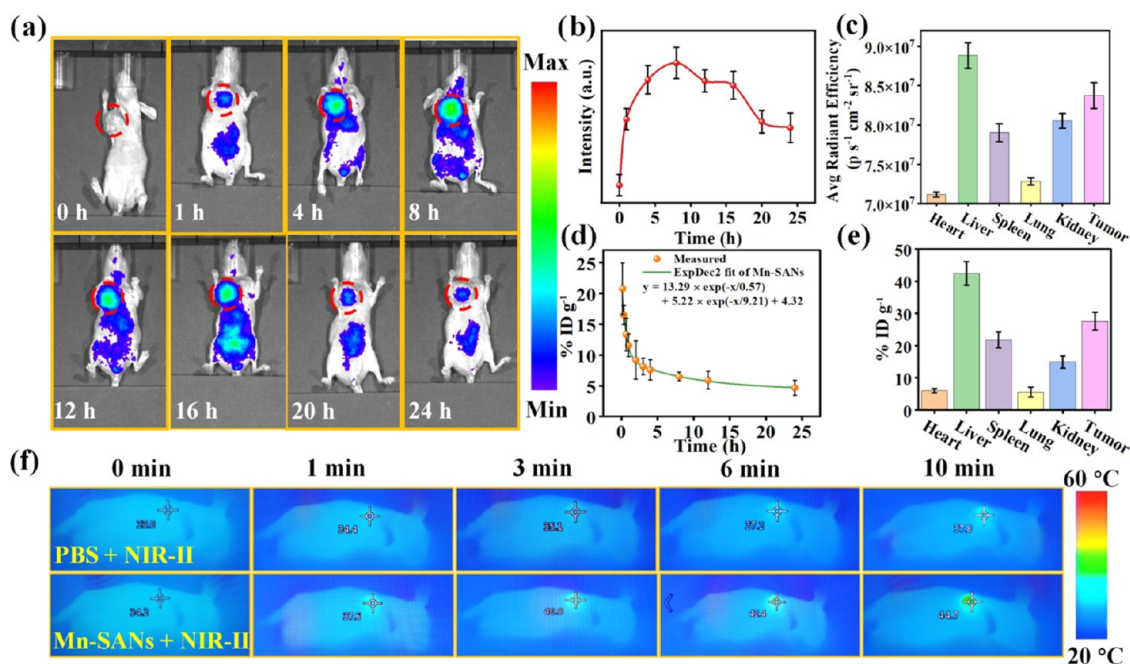


Figure 6. (a) *In vivo* fluorescence images of Saos-2 tumor-bearing mice after i.v. administration of ICG-labeled Mn-SANs. (b) Fluorescence intensity extracted from tumor regions as a function of time after administration of ICG-labeled Mn-SANs. (c) *Ex vivo* quantification of average fluorescence intensity of the major organs and tumor of mice at 24 h after administration of ICG-labeled Mn-SANs. (d) Mn concentrations in the blood from mice treated with Mn-SANs. (e) *In vivo* distribution of Mn in main organs and tumors after 24 h of Mn-SAN treatment. (f) Thermal images of Saos-2-tumor-bearing mice injected with PBS and Mn-SANs upon NIR-II laser irradiation. ($n = 3$, mean \pm SD; *** $p < 0.001$, ** $p < 0.01$, and * $p < 0.05$).

to Saos-2 cells, stemming from mild PTT. Mn-SANs also had an obvious lethal effect for Saos-2 cells, attributing to plentiful $\cdot\text{O}_2^-$ generation and LPO-featured ferroptosis triggered by their multienzyme activities. Compared with other treatment groups, the Mn-SANs + NIR-II group achieved an impressive therapeutic effect due to the synergies of the mild photothermal effect and multienzyme catalysis, which basically killed all Saos-2 cells, with the survival rate as low as 2.7%. Taken together, these results were further sanctioned by live/dead imaging (Figure 5f). Flow cytometer apoptotic analysis of Saos-2 cells also provided confirmation (Figure 5g). Therefore, such synergistic mild photothermal/multienzymatic therapy mediated by Mn-SANs possessed the potential to enhance antiosteosarcoma efficacy through a two-pronged strategy of chemical processes and biological processes.

2.3. *In Vivo* Synergistic Osteosarcoma Eradication.

The excellent *in vitro* synergistic treatment property of Mn-SANs encouraged us to further investigate the *in vivo* antiosteosarcoma effect on Saos-2 tumor-bearing mice. Before that, the biodistribution of Mn-SANs was explored. After the i.v. administration of ICG-labeled Mn-SANs into Saos-2 tumor-bearing mice, ICG intensity can be witnessed in the tumor regions and reached its maximum at 8 h, being sustained for a further 24 h, highlighting the effective tumor enrichment features of Mn-SANs (Figure 6a,b). Furthermore, as shown in the *ex vivo* fluorescence image of the excised tumor, the liver, kidney, and spleen showed relatively higher fluorescence compared with the heart and lung, indicating the active uptake by the reticuloendothelial system (Figure 6c). Next, the half-life of Mn-SANs in the bloodstream of Saos-2 tumor-bearing mice was calculated to be 1.38 h by detecting the concentration of Mn in the blood over time (Figure 6d). Additionally, the *in vivo* distribution of Mn in main organs and

tumors after 24 h of Mn-SAN injection suggested a significant intratumoral enrichment of Mn-SANs (Figure 6e). Subsequently, *in vivo* photothermal effects of Mn-SANs were evaluated by monitoring thermal images and the temperature variation of the tumor sites under NIR-II irradiation (Figure 6f). As revealed in the infrared imaging, the local tumor temperature of Saos-2 tumor-bearing mice treated with Mn-SANs was elevated to 44.7 °C within 10 min by altering a suitable laser power density, thereby offering a relatively safe mild temperature for therapy.

Based on the remarkable *in vitro* antiosteosarcoma effects, satisfactory tumor accumulation, and favorable *in vivo* photothermal effects, the antiosteosarcoma performance of Mn-SANs was further studied in Saos-2 tumor-bearing mice for 14 days. The tumors were then treated with PBS + NIR-II, UCNs + NIR-II, Mn-SANs, and Mn-SANs + NIR-II groups. Within 2 weeks of therapy, the tumor volume of all mice was measured every other day (Figure 7a). Compared with PBS + NIR-II, UCNs + NIR-II, and Mn-SANs, tumors in the Mn-SANs + NIR-II treatment group were substantially inhibited with no obvious tumor growth found during the treatment period. After 14 days, mice were sacrificed; the tumors were resected and weighed, and the inhibition rate was calculated accordingly. Photographs of excised osteosarcoma further confirmed that synergistic mild photothermal/multienzymatic therapy mediated by Mn-SANs had a significant inhibitory effect on osteosarcoma (Figure 7b). Next, according to quantitative analysis of weight and inhibition rate for osteosarcoma (Figure 7c,d), the tumors in the Mn-SANs and UCNs + NIR-II groups were only partially suppressed and still increased at a certain rate, with the tumor inhibition rates of ~ 39.5 and $\sim 24.2\%$, respectively. It was worth noting that the tumors in the Mn-SANs + NIR-II group were almost

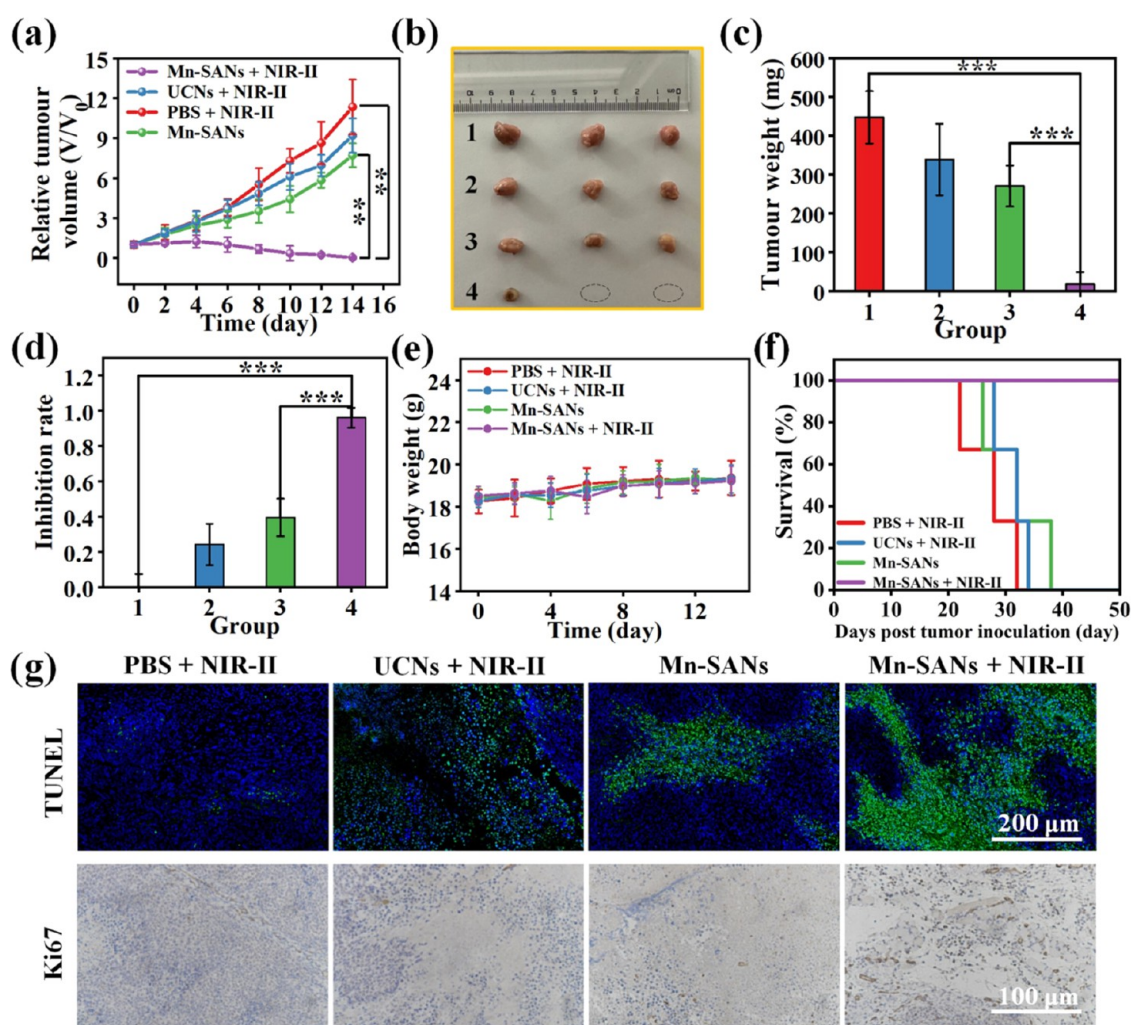


Figure 7. (a) Growth curves of osteosarcoma in Saos-2 tumor-bearing mice after various therapies. (b) Photographs of excised osteosarcoma from different treatments. (c) Osteosarcoma weight separated from Saos-2 tumor-bearing mice after various therapies. (d) Inhibition rate of all groups with that of the control group as zero. (e) Body weights of mice in different groups. (f) Survival profiles of mice in various groups. (g) Pathological results of mice in different groups via TUNEL and antigen K_i -67 staining. Groups: (1) PBS + NIR-II, (2) UCNs + NIR-II, (3) Mn-SANs, and (4) Mn-SANs + NIR-II. ($n = 3$, mean \pm SD; *** $p < 0.001$, ** $p < 0.01$, and * $p < 0.05$).

completely eradicated with the inhibition rate of up to 96.9%. This resulted from synergistic mild photothermal/multi-enzymatic therapy achieved by a two-pronged strategy of chemical processes and biological processes mediated by Mn-SANs. Meanwhile, the Mn-SANs + NIR-II treatment led to no evident body weight loss issues (Figure 7e). Besides, all the mice in PBS + NIR-II, UCNs + NIR-II, and Mn-SAN groups died at day 40 (Figure 7f). In contrast, mice in the Mn-SANs + NIR-II group survived for over 50 days, with the survival rate as high as 100%, indicating that the Mn-SAN-mediated synergistic mild photothermal/multi-enzymatic therapy had a satisfactory inhibitory effect on tumor growth. Moreover, pathological assays, including terminal deoxynucleotidyl transferase dUTP nick end label (TUNEL) staining and K_i -67 staining, further confirmed the outstanding antiosteosarcoma effect of synergistic mild photothermal/multi-enzymatic therapy (Figure 7g). After Mn-SANs + NIR-II treatment, the hematoxylin-eosin (H&E) staining images showed no obvious injury in major organs including the heart, liver, spleen, lungs, and kidneys (Figure S7). In addition, the biochemical blood indices of mice showed no significant differences after 14 days of the treatment with Mn-SANs and PBS, respectively (Figure

S8). Therefore, these results indicated that the Mn-SAN-mediated synergistic mild photothermal/multi-enzymatic therapy not only exhibited excellent inhibition of tumor growth but also showed negligible toxicity.

3. CONCLUSIONS

In summary, we developed efficient SANs consisting of Mn sites atomically dispersed on nitrogen-doped carbon nanosheets for synergistic mild photothermal/multi-enzymatic therapy against osteosarcoma. The resulting Mn-SANs showed a remarkable photothermal effect in the near-infrared II (NIR-II, 1000–1400 nm) region and excellent synergistic multi-enzyme properties. On the one hand, owing to their black N-doped carbon nanosheet matrices, Mn-SANs possessed strong optical absorption and exhibited excellent NIR-II-triggered photothermal performance. Moreover, by adjusting laser power density, Mn-SANs can give a relatively safe mild treatment temperature. On the other hand, Mn-SANs can catalyze endogenous H_2O_2 in osteosarcoma into O_2 by CAT-like activity, excellently easing osteosarcoma low-oxygen conditions and activating the OXD-like catalysis that converted O_2 to cytotoxic $\bullet O_2$. Meanwhile, Mn-SANs can also mimic GSHOx

to effectively consume the antioxidant GSH in the TME and inhibit the intracellular GPX4 expression. Such intratumoral $\cdot\text{O}_2^-$ production, GSH depletion, and GPX4 inactivation mediated by Mn-SANs can create a large accumulation of LPO and $\cdot\text{O}_2^-$, leading to oxidative stress and disrupting the redox homeostasis in tumor cells, which ultimately induced tumor cell death. More importantly, HSPs can be significantly destroyed through Mn-SAN-mediated plentiful LPO and ROS generation, thus effectively impairing tumor cells resistant to mild PTT. Additionally, the photothermal effect triggered by Mn-SANs can further enhance multienzyme activities to boost $\cdot\text{O}_2^-$ generation, GSH depletion, and LPO accumulation. Finally, through a two-pronged strategy of chemical processes and biological processes, synergistic mild photothermal/multienzymatic therapy mediated by Mn-SANs exhibited a significantly enhanced antiosteosarcoma efficacy.

4. EXPERIMENTAL SECTION

4.1. Synthesis of Mn-SANs. The precursor for the Mn-BTC MOF ($\text{Mn}(\text{BTC})(\text{H}_2\text{O})_3$) was initially synthesized through chemical precipitation, employing trimesic acid and manganese acetate in a water–ethanol solvent. Specifically, a solution comprising $\text{Mn}(\text{CH}_3\text{COO})_2 \cdot 4\text{H}_2\text{O}$ (0.488 g) and trimesic acid (0.232g) was dissolved in a 200 mL ethanol–water mixture and stirred at room temperature for 2 h. The resulting product underwent centrifugation, thorough washing with deionized water, and subsequent drying in a vacuum oven for 24 h to yield the Mn-BTC MOF precursor.

The 0.1 g portion of the Mn-BTC MOF precursor was sufficiently ground and mixed with dicyandiamide to form a homogenous mixture. Subsequently, the obtained product underwent pyrolysis in a tube furnace at 800 °C under a N_2 flow for 3 h. The resulting pyrolysis product was washed with deionized water/ethanol and diluted with acid under ultrasound to eliminate metal and dicyandiamide residues.

4.2. Measurement of Multienzyme-Like Activity. To assess the CAT-like activity of Mn-SANs, the oxygen production was measured. Briefly, Mn-SANs ($60 \mu\text{g mL}^{-1}$) were incubated with varying concentrations of H_2O_2 (0, 1, 3, and 5 mM) in a PBS solution (pH = 6.0). Subsequently, the oxygen concentrations were monitored in real time for 6 min.

The DPBF was employed to determine the presence of $\cdot\text{O}_2^-$. Briefly, DPBF and different samples were mixed in PBS solution (pH = 6.0). The degree of $\cdot\text{O}_2^-$ was determined by the degradation in absorbance at 420 nm.

To explore the GSHOx-like activity, Mn-SANs ($60 \mu\text{g mL}^{-1}$) were incubated with GSH in PBS solution (pH 6.0). At the corresponding time points, DTNB was used as a probe to measure the remaining GSH and record the absorbance with a UV–vis spectrophotometer.

4.3. Detection of Intracellular $\cdot\text{O}_2^-$ and GSH. For the detection of intracellular $\cdot\text{O}_2^-$, Saos-2 cells were treated with various conditions, and DCFH-DA was used to stain the cells. The fluorescence signal intensity of DCF reflects intracellular $\cdot\text{O}_2^-$ levels. To assess the mitochondrial membrane potential, JC-1 was employed to stain Saos-2 cells post-treatment. A red signal for JC-1 aggregates or a green signal for JC-1 monomers indicated normal or reduced mitochondrial membrane potential. To detect intracellular GSH, Saos-2 cells were cultured in 96-well plates and subjected to different treatments: PBS-only, NIR-II-only, UCNs + NIR-II, Mn-SAN, or Mn-SANs + NIR-II groups. Following treatment, each group

of GSH levels was analyzed using the GSH assay kit according to the manufacturer's instructions.

4.4. Cell Viability Assay. To assess the antiosteosarcoma effects of various treatments *in vitro*, cell toxicity experiments were organized into five groups: (1) PBS only, (2) NIR-II only, (3) UCNs + NIR-II, (4) Mn-SANs, and (5) Mn-SANs + NIR-II. The Mn-SANs and UCNs were present at an equivalent concentration of $150 \mu\text{g mL}^{-1}$ in all groups. Saos-2 cells were treated with different treatments, including 0.1 mM H_2O_2 . After 6 h of incubation, the irradiation groups were subjected to a 1064 nm laser. Subsequently, the cells were further cultured for 24 h. Finally, the cell viability was assessed by CCK-8 assay in different groups of treatments. Furthermore, Saos-2 cells were stained with calcein-AM and PI to confirm treated live/dead cells. After that, the treated Saos-2 cells were further stained with Annexin V-FITC and PI staining kits and sorted by flow cytometry.

4.5. In Vivo Antiosteosarcoma Performance. All animal experiments adhered to the relevant laws and institutional guidelines of the University of Chinese Academy of Sciences (UCAS) and received approval from the Model Animal Research Center of the Institute of Process Engineering, Chinese Academy of Sciences. Female Balb/c nude mice were obtained from Beijing HFK Bioscience Co., Ltd. Each mouse received a subcutaneous injection of 4×10^6 Saos-2 cells in the right scapular region. The treatment was initiated when Saos-2 tumor-bearing mice reached a tumor volume of 80–100 mm^3 . For *in vivo* infrared thermography, 8 h postinjection of Mn-SANs (15 mg kg^{-1}) or PBS, the tumor area underwent irradiation with a 1064 nm laser. An infrared thermal imaging camera was employed to record real-time temperature changes and infrared thermal images of the mice. For *in vivo* antiosteosarcoma experiments, Saos-2 tumor-bearing mice were divided into four groups, with three mice in each group: (1) PBS + NIR-II; (2) UCNs + NIR-II; (3) Mn-SANs; and (4) Mn-SANs + NIR-II. The equivalent doses of intravenously injected Mn-SANs and UCNs in different groups were approximately 15 mg kg^{-1} . The irradiation group was exposed to 1064 nm laser 8 h after intravenous injection. Tumor size and body weight of animals in four groups were recorded every 2 days over the 14-day treatment period. Following treatment for 14 days, the mice were euthanized, and tumor tissues were harvested and weighed. In addition, the mouse tissue sections were processed for hematoxylin–eosin (H&E), terminal deoxynucleotidyl transferase-mediated dUTP nickel-end labeling (TUNEL), and Ki67 staining to investigate histological differences.

■ ASSOCIATED CONTENT

SI Supporting Information

The Supporting Information is available free of charge at <https://pubs.acs.org/doi/10.1021/acsomega.3c07714>.

Photothermal performance, ζ -potential, and stability of nanozymes, H&E staining of the main organs, materials, synthesis of Mn-SANs, PEG modification of Mn-SANs, photothermal performance of Mn-SANs, measurement of CAT-like activity, measurement of OXD-like activity, measurement of GSHOx-like activity, characterization, biocompatibility assay, detection of intracellular $\cdot\text{O}_2^-$ and GSH, cell viability assay, western blot assays, pharmacokinetics, biodistribution, and *in vivo* antiosteosarcoma performance (PDF)

AUTHOR INFORMATION

Corresponding Authors

Shan He – School of Light Industry, Beijing Technology and Business University, Beijing 100048, China; orcid.org/0000-0002-1183-6917; Email: vh30@163.com

Xiao-bo Luo – Department of Orthopedics, The Eighth Medical Center of the Chinese PLA General Hospital, Beijing 100091, China; Department of Orthopedics, The Fourth Medical Center of the Chinese PLA General Hospital, Beijing 100037, China; Email: uoxiaobo_309@163.com

Authors

Cun-shuo Wang – Department of Graduate, Hebei North University, Zhangjiakou 075000 Hebei, China; Department of Orthopedics, The Eighth Medical Center of the Chinese PLA General Hospital, Beijing 100091, China

Hai-bin Xue – Department of Orthopedics, The Eighth Medical Center of the Chinese PLA General Hospital, Beijing 100091, China; Department of Orthopedics, The Fourth Medical Center of the Chinese PLA General Hospital, Beijing 100037, China

Liang Zhuang – School of Light Industry, Beijing Technology and Business University, Beijing 100048, China

Hai-peng Sun – Department of Graduate, Hebei North University, Zhangjiakou 075000 Hebei, China; Department of Orthopedics, The Eighth Medical Center of the Chinese PLA General Hospital, Beijing 100091, China

Hua Zheng – Department of Graduate, Hebei North University, Zhangjiakou 075000 Hebei, China; Department of Orthopedics, The Eighth Medical Center of the Chinese PLA General Hospital, Beijing 100091, China

Shuai Wang – Department of Orthopedics, The Eighth Medical Center of the Chinese PLA General Hospital, Beijing 100091, China; Department of Orthopedics, The Fourth Medical Center of the Chinese PLA General Hospital, Beijing 100037, China

Complete contact information is available at:

<https://pubs.acs.org/10.1021/acsomega.3c07714>

Author Contributions

¹C.-s.W., H.-b.X., and L.Z. contributed equally to this work. The article was written through contributions of all authors. All authors have given approval to the final version of the article.

Notes

The authors declare no competing financial interest.

ACKNOWLEDGMENTS

The authors thank the R&D Program of the Beijing Municipal Education Commission (KZ202210011015). The authors are thankful for the support of the BSRF (Beijing Synchrotron Radiation Facility) during the XAFS measurements.

REFERENCES

- (1) Wang, L. Y.; Yang, Q. H.; Huo, M. F.; Lu, D.; Gao, Y. S.; Chen, Y.; Xu, H. X. Engineering single-atomic Iron-Catalyst-Integrated 3D-Printed bioscaffolds for osteosarcoma destruction with antibacterial and bone defect regeneration bioactivity. *Adv. Mater.* **2021**, *33*, No. 2100150.
- (2) Kansara, M.; Teng, M. W.; Smyth, M. J.; Thomas, D. M. Translational biology of osteosarcoma. *Nat. Rev. Cancer* **2014**, *14*, 722–735.
- (3) Chen, Y.; Di Grappa, M. A.; Molyneux, S. D.; McKee, T. D.; Waterhouse, P.; Penninger, J. M.; Khokha, R. RANKL blockade

prevents and treats aggressive osteosarcomas. *Sci. Transl. Med.* **2015**, *7*, 197r–317r.

(4) Grimer, R. J. Surgical options for children with osteosarcoma. *Lancet Oncol.* **2005**, *6*, 85–92.

(5) Liu, Y. J.; Bhattarai, P.; Dai, Z. F.; Chen, X. Y. Photothermal therapy and photoacoustic imaging via nanotheranostics in fighting cancer. *Chem. Soc. Rev.* **2019**, *48*, 2053–2108.

(6) Chang, M. Y.; Hou, Z. Y.; Wang, M.; Yang, C. Z.; Wang, R. F.; Li, F.; Liu, D. L.; Peng, T. L.; Li, C. X.; Lin, J. Single-Atom Pd nanozyme for Ferroptosis-Boosted Mild-Temperature photothermal therapy. *Angew. Chem., Int. Ed.* **2021**, *60*, 12971–12979.

(7) Ma, G. C.; Liu, Z. K.; Zhu, C. G.; Chen, H. J.; Kwok, R. T. K.; Zhang, P. F.; Tang, B. Z.; Cai, L. T.; Gong, P. H₂O₂-Responsive NIR-II AIE Nanobomb for Carbon Monoxide Boosting Low-Temperature Photothermal Therapy. *Angew. Chem., Int. Ed.* **2022**, *61*, No. e202207213.

(8) Yu, Z. Z.; Chan, W. K.; Zhang, Y.; Tan, T. T. Y. Near-infrared-II activated inorganic photothermal nanomedicines. *Biomaterials* **2021**, *269*, No. 120459.

(9) Li, S. S.; Gu, K.; Wang, H.; Xu, B. L.; Li, H. W.; Shi, X. H.; Huang, Z. J.; Liu, H. Y. Degradable Holey Palladium Nanosheets with Highly Active 1D Nanoholes for Synergetic Phototherapy of Hypoxic Tumors. *J. Am. Chem. Soc.* **2020**, *142*, 5649–5656.

(10) Huang, L. P.; Li, Y. N.; Du, Y. N.; Zhang, Y. Y.; Wang, X. X.; Ding, Y.; Yang, X. L.; Meng, F. L.; Tu, J. S.; Luo, L.; Sun, C. M. Mild photothermal therapy potentiates anti-PD-L1 treatment for immunologically cold tumors via an all-in-one and all-in-control strategy. *Nat. Commun.* **2019**, *10*, No. 4871, DOI: [10.1038/s41467-019-12771-9](https://doi.org/10.1038/s41467-019-12771-9).

(11) Gao, G.; Sun, X. B.; Liang, G. L. Nanoagent-Promoted Mild-Temperature Photothermal Therapy for Cancer Treatment. *Adv. Funct. Mater.* **2021**, *31*, No. 2100738.

(12) Yang, K.; Zhao, S. J.; Li, B. L.; Wang, B. H.; Lan, M. H.; Song, X. Z. Low temperature photothermal therapy: Advances and perspectives. *Coord. Chem. Rev.* **2022**, *454*, No. 214330.

(13) Yang, Y.; Zhu, W. J.; Dong, Z. L.; Chao, Y.; Xu, L.; Chen, M. W.; Liu, Z. 1D Coordination Polymer Nanofibers for Low-Temperature Photothermal Therapy. *Adv. Mater.* **2017**, *29*, No. 1703588.

(14) Li, B.; Hao, G. Y.; Sun, B.; Gu, Z.; Xu, Z. P. Engineering a Therapy-Induced "Immunogenic Cancer Cell Death" Amplifier to Boost Systemic Tumor Elimination. *Adv. Funct. Mater.* **2020**, *30*, No. 1909745, DOI: [10.1002/adfm.201909745](https://doi.org/10.1002/adfm.201909745).

(15) Zhang, B.; Shao, C. W.; Zhou, K. M.; Li, Q.; Duan, Y. T.; Yang, Y. S.; Zhu, H. L. A NIR-triggered multifunctional nanoplatform mediated by Hsp70 siRNA for chemo-hypothermal photothermal synergistic therapy. *Biomater. Sci.* **2021**, *9*, 6501–6509.

(16) Wang, Y. C.; Dai, X. Y.; Dong, C. H.; Guo, W. T.; Xu, Z. W.; Chen, Y.; Xiang, H. J.; Zhang, R. F. Engineering Electronic Band Structure of Binary Thermoelectric Nanocatalysts for Augmented Pyrocatalytic Tumor Nanotherapy. *Adv. Mater.* **2022**, *34*, No. 2106773.

(17) Jiang, Z. Q.; Yuan, B.; Wang, Y. J.; Wei, Z. N.; Sun, S.; Akakuru, O. U.; Li, Y.; Li, J.; Wu, A. G. Near-infrared heptamethine cyanine dye-based nanoscale coordination polymers with intrinsic nucleus-targeting for low temperature photothermal therapy. *Nano Today* **2020**, *34*, No. 100910.

(18) Huang, Y. Y.; Ren, J. S.; Qu, X. G. Nanozymes: Classification, Catalytic Mechanisms, Activity Regulation, and Applications. *Chem. Rev.* **2019**, *119*, 4357–4412.

(19) Ai, Y. J.; Hu, Z. N.; Liang, X. P.; Sun, H. B.; Xin, H. B.; Liang, Q. L. Recent Advances in Nanozymes: From Matters to Bioapplications. *Adv. Funct. Mater.* **2022**, *32*, No. 2110432.

(20) Hu, X.; Li, F. Y.; Xia, F.; Guo, X.; Wang, N.; Liang, L. L.; Yang, B.; Fan, K. L.; Yan, X. Y.; Ling, D. S. Biodegradation-Mediated Enzymatic Activity-Tunable Molybdenum Oxide Nanourchins for Tumor-Specific Cascade Catalytic Therapy. *J. Am. Chem. Soc.* **2020**, *142*, 1636–1644.

- (21) Jana, D.; He, B.; Chen, Y.; Liu, J.; Zhao, Y. A Defect-Engineered Nanozyme for Targeted NIR-II Photothermal Immunotherapy of Cancer. *Adv. Mater.* **2022**, No. 2206401.
- (22) Dong, S.; Dong, Y.; Zhao, Z.; Liu, J.; Liu, S.; Feng, L.; He, F.; Gai, S.; Xie, Y.; Yang, P. Electron Transport Chain Interference” Strategy of Amplified Mild-Photothermal Therapy and Defect-Engineered Multi-Enzymatic Activities for Synergistic Tumor-Personalized Suppression. *J. Am. Chem. Soc.* **2023**, *145*, 9488–9507.
- (23) Zhao, S.; Li, H.; Liu, R.; Tao, N.; Deng, L.; Xu, Q.; Hou, J.; Sheng, J.; Zheng, J.; Wang, L.; Chen, W.; Guo, S.; Liu, Y.-N. Nitrogen-Centered Lactate Oxidase Nanozyme for Tumor Lactate Modulation and Microenvironment Remodeling. *J. Am. Chem. Soc.* **2023**, *145*, 10322–10332.
- (24) Chao, S.; Shen, Z. Y.; Pei, Y. X.; Lv, Y. H.; Chen, X. L.; Ren, J. M.; Yang, K.; Pei, Z. C. Pillar[5]arene-based supramolecular photosensitizer for enhanced hypoxic-tumor therapeutic effectiveness. *Chem. Commun.* **2021**, *57*, 7625–7628.
- (25) Yu, B.; Wang, W.; Sun, W. B.; Jiang, C. H.; Lu, L. H. Defect Engineering Enables Synergistic Action of Enzyme-Mimicking Active Centers for High-Efficiency Tumor Therapy. *J. Am. Chem. Soc.* **2021**, *143*, 8855–8865.
- (26) Liu, Y.; Wang, B.; Zhu, J. J.; Xu, X. N.; Zhou, B.; Yang, Y. Single-Atom Nanozyme with Asymmetric Electron Distribution for Tumor Catalytic Therapy by Disrupting Tumor Redox and Energy Metabolism Homeostasis. *Adv. Mater.* **2023**, *35*, No. 2208512.
- (27) Cai, S. F.; Liu, J. M.; Ding, J. W.; Fu, Z.; Li, H. L.; Xiong, Y. L.; Lian, Z.; Yang, R.; Chen, C. Y. Tumor-Microenvironment-Responsive Cascade Reactions by a Cobalt-Single-Atom Nanozyme for Synergistic Nanocatalytic Chemotherapy. *Angew. Chem., Int. Ed.* **2022**, *61*, No. e202204502.
- (28) Chang, M. Y.; Hou, Z. Y.; Wang, M.; Wen, D.; Li, C. X.; Liu, Y. H.; Zhao, Y. L.; Lin, J. Cu Single Atom Nanozyme Based High-Efficiency Mild Photothermal Therapy through Cellular Metabolic Regulation. *Angew. Chem., Int. Ed.* **2022**, *61*, No. e202209245.
- (29) Dong, Z.; Liang, P.; Guan, G. Q.; Yin, B. L.; Wang, Y. J.; Yue, R. Y.; Zhang, X. B.; Song, G. S. Overcoming Hypoxia-Induced Ferroptosis Resistance via a F-19/H-1-MRI Traceable Core-Shell Nanostructure. *Angew. Chem., Int. Ed.* **2022**, *61*, No. e202206074, DOI: 10.1002/anie.202206074.
- (30) Feng, W.; Liu, Z. L.; Xia, L. L.; Chen, M.; Dai, X. Y.; Huang, H.; Dong, C. H.; He, Y.; Chen, Y. A Sonication-Activated Valence-Variable Sono-Sensitizer/Catalyst for Autophagy Inhibition/Ferroptosis-Induced Tumor Nanotherapy. *Angew. Chem., Int. Ed.* **2022**, *61*, No. e202212021.
- (31) Zhu, Y.; Wang, W. Y.; Cheng, J. J.; Qu, Y. T.; Dai, Y.; Liu, M. M.; Yu, J. N.; Wang, C. M.; Wang, H. J.; Wang, S. C.; Zhao, C.; Wu, Y.; Liu, Y. Z. Stimuli-Responsive Manganese Single-Atom Nanozyme for Tumor Therapy via Integrated Cascade Reactions. *Angew. Chem., Int. Ed.* **2021**, *60*, 9480–9488.
- (32) Jiao, L.; Yan, H. Y.; Wu, Y.; Gu, W. L.; Zhu, C. Z.; Du, D.; Lin, Y. H. When Nanozymes Meet Single-Atom Catalysis. *Angew. Chem., Int. Ed.* **2020**, *59*, 2565–2576.
- (33) Qiu, J. J.; Geng, H.; Wang, D. H.; Qian, S.; Zhu, H. Q.; Qiao, Y. Q.; Qian, W. H.; Liu, X. Y. Layer-Number Dependent Antibacterial and Osteogenic Behaviors of Graphene Oxide Electrophoretic Deposited on Titanium. *ACS Appl. Mater. Interfaces* **2017**, *9*, 12253–12263.
- (34) Xu, B. L.; Wang, H.; Wang, W. W.; Gao, L. Z.; Li, S. S.; Pan, X. T.; Wang, H. Y.; Yang, H. L.; Meng, X. Q.; Wu, Q. W.; Zheng, L. R.; Chen, S. M.; Shi, X. H.; Fan, K. L.; Yan, X. Y.; Liu, H. Y. A Single-Atom Nanozyme for Wound Disinfection Applications. *Angew. Chem., Int. Ed.* **2019**, *58*, 4911–4916.
- (35) Cui, T. T.; Wang, Y. P.; Ye, T.; Wu, J.; Chen, Z. Q.; Li, J.; Lei, Y. P.; Wang, D. S.; Li, Y. D. Engineering Dual Single-Atom Sites on 2D N-doped Carbon Nanosheets Attaining Ultra-Low-Temperature Zinc-Air Battery. *Angew. Chem., Int. Ed.* **2022**, *61*, No. e202115219, DOI: 10.1002/anie.202115219.
- (36) Wang, L. M.; Chen, W. L.; Zhang, D. D.; Du, Y. P.; Amal, R.; Qiao, S. Z.; Bf, J. W.; Yin, Z. Y. Surface strategies for catalytic CO₂ reduction: from two-dimensional materials to nanoclusters to single atoms. *Chem. Soc. Rev.* **2019**, *48*, 5310–5349.
- (37) Li, K. L.; Ma, X. T.; He, S.; Wang, L.; Yang, X. T.; Zhang, G. J.; Guan, S. Y.; Qu, X. Z.; Zhou, S. Y.; Xu, B. C. Nanosheet-Supported Ag@Ag₂O Core-Shell Nanoparticles with Vastly Enhanced Photothermal Conversion Efficiency for NIR-II-Triggered Photothermal Therapy. *ACS Biomater. Sci. Eng.* **2022**, *8*, 540–550.
- (38) Zheng, T. T.; Jiang, K.; Ta, N.; Hu, Y. F.; Zeng, J.; Liu, J. Y.; Wang, H. T. Large-Scale and Highly Selective CO₂ Electrocatalytic Reduction on Nickel Single-Atom Catalyst. *Joule* **2019**, *3*, 265–278.
- (39) Zhu, W. J.; Zhang, L.; Liu, S. H.; Li, A.; Yuan, X. T.; Hu, C. L.; Zhang, G.; Deng, W. Y.; Zang, K. T.; Luo, J.; Zhu, Y. M.; Gu, M.; Zhao, Z. J.; Gong, J. L. Enhanced CO₂ Electroreduction on Neighboring Zn/Co Monomers by Electronic Effect. *Angew. Chem., Int. Ed.* **2020**, *59*, 12664–12668.
- (40) Baer, D. R.; Blanchard, D. L.; Engelhard, M. H.; Zachara, J. M. The interaction of water and Mn with surfaces of CaCO₃: an XPS study. *Surf. Interface Anal.* **1991**, *17*, 25–30.
- (41) Yang, Y. Q.; Fan, X. X.; Li, L.; Yang, Y. M.; Nuernisha, A.; Xue, D. W.; He, C.; Qian, J.; Hu, Q. L.; Chen, H.; Liu, J.; Huang, W. Semiconducting Polymer Nanoparticles as Theranostic System for Near-Infrared-II Fluorescence Imaging and Photothermal Therapy under Safe Laser Fluence. *ACS Nano* **2020**, *14*, 2509–2521.
- (42) Yang, Y.; Chen, M.; Wang, B. Z.; Wang, P.; Liu, Y. C.; Zhao, Y.; Li, K.; Song, G. S.; Zhang, X. B.; Tan, W. H. NIR-II Driven Plasmon-Enhanced Catalysis for a Timely Supply of Oxygen to Overcome Hypoxia-Induced Radiotherapy Tolerance. *Angew. Chem., Int. Ed.* **2019**, *58*, 15069–15075.
- (43) Zhou, Z.; Wang, Y. L.; Peng, F.; Meng, F.; Zha, J.; Ma, L.; Du, Y.; Peng, N.; Ma, L.; Zhang, Q.; Gu, L.; Yin, W.; Gu, Z.; Tan, C. Intercalation-Activated Layered MoO₃ Nanobelts as Biodegradable Nanozymes for Tumor-Specific Photo-Enhanced Catalytic Therapy. *Angew. Chem., Int. Ed.* **2022**, *61*, No. e202115939, DOI: 10.1002/anie.202115939.
- (44) Peng, C.; Liu, J.; Guo, L.; Bai, J.; Zhou, M. Oxygen Vacancy-Enhanced Photothermal Performance and Reactive Oxygen Species Generation for Synergistic Tumour Therapy. *Chem. Commun.* **2020**, *56*, 11259–11262.
- (45) Dong, S.; Dong, Y.; Jia, T.; Liu, S.; Liu, J.; Yang, D.; He, F.; Gai, S.; Yang, P.; Lin, J. GSH-Depleted Nanozymes with Hyperthermia-Enhanced Dual Enzyme-Mimic Activities for Tumor Nanocatalytic Therapy. *Adv. Mater.* **2020**, *32*, No. 2002439.
- (46) Fan, L.; Xu, X.; Zhu, C.; Han, J.; Gao, L.; Xi, J.; Guo, R. Tumor Catalytic-Photothermal Therapy with Yolk-Shell Gold@Carbon Nanozymes. *ACS Appl. Mater. Interfaces* **2018**, *10*, 4502–4511.
- (47) Wu, Y.; Tang, Y.; Xu, W.; Su, R.; Qin, Y.; Jiao, L.; Wang, H.; Cui, X.; Zheng, L.; Wang, C.; Hu, L.; Gu, W.; Du, D.; Lin, Y.; Zhu, C. Photothermal-Switched Single-Atom Nanozyme Specificity for Pretreatment and Sensing. *Small* **2023**, *19*, No. 2302929.
- (48) Dong, S. M.; Dong, Y. S.; Zhao, Z. Y.; Liu, J.; Liu, S. K.; Feng, L. L.; He, F.; Gai, S. L.; Xie, Y.; Yang, P. P. Electron Transport Chain Interference” Strategy of Amplified Mild-Photothermal Therapy and Defect-Engineered Multi-Enzymatic Activities for Synergistic Tumor-Personalized Suppression. *J. Am. Chem. Soc.* **2023**, *145*, 9488–9507.
- (49) Lu, S. J.; Tian, H. L.; Li, L.; Li, B. W.; Yang, M.; Zhou, L.; Jiang, H.; Li, Q.; Wang, W. H.; Nice, E. C.; Xie, N.; Huang, C. H.; Liu, L. Nanoengineering a Zeolitic Imidazolate Framework-8 Capable of Manipulating Energy Metabolism against Cancer Chemo-Phototherapy Resistance. *Small* **2022**, *18*, No. 2204926.